Optical and thermoelectric properties of non-Janus CuI and AgI, and Janus Cu_2BrI and Ag_2BrI monolayers by many-body perturbation theory

Mohammad Ali Mohebpour,[1,*] Bohayra Mortazavi,[2,†] Xiaoying Zhuang,[2] and Meysam Bagheri Tagani[1,‡]
[1]*Department of Physics, University of Guilan, P. O. Box 41335-1914, Rasht, Iran*
[2]*Department of Mathematics and Physics, Leibniz Universität Hannover, Appelstraβe 11, 30167 Hannover, Germany*

(Received 21 April 2022; revised 30 July 2022; accepted 25 August 2022; published 7 September 2022)

In an outstanding experimental advance in the field of two-dimensional nanomaterials, cuprous iodide (CuI) and silver iodide (AgI) monolayers have been grown via a novel graphene encapsulation synthesis approach [K. Mustonen *et al.*, Adv. Mater. **34**, 2106922 (2022)]. Inspired by this accomplishment, we conduct first-principles calculations to investigate the elastic, phonon, and electron thermal transport, electronic, and optical properties of the non-Janus CuI and AgI and Janus Cu_2BrI and Ag_2BrI monolayers. Electronic and excitonic optical properties are elaborately studied using the many-body perturbation theory on the basis of *GW* approximation. Our results indicate that these novel systems are stable but with soft elastic modulus and ultralow lattice thermal conductivity. It is also shown that the studied monolayers are wide-gap semiconductors with exciton binding energies close to 1 eV. The spin-orbit induced band splitting of Janus monolayers are increased more than 100% under a uniaxial strain of 3%, and for non-Janus monolayers, a noticeable increase is observed under a perpendicular electric field. Thermoelectric efficiency of silver-based monolayers is higher than 1.2, making them promising candidates for next-generation thermoelectric devices. The presented first-principles results provide a deep understanding of the stability, thermal transport, and tunable optoelectronic properties of CuI, AgI, Cu_2BrI, and Ag_2BrI monolayers, which can serve as a guide for the oncoming studies.

DOI: 10.1103/PhysRevB.106.125405

I. INTRODUCTION

Two-dimensional (2D) materials have attracted the interest of researchers in recent years, for developing next-generation optoelectronic and energy storage/conversion devices due to their outstanding physical properties. Graphene, the most famous 2D material, has been proven to strongly interact with light from microwave to ultraviolet wavelengths, exhibiting wide applications in optoelectronic devices [1]. To improve the efficiency of optoelectronic devices, novel layered 2D materials have been experimentally synthesized such as transition metal dichalcogenide (TMD) monolayers (like MoS_2 [2], WS_2 [3], and WSe_2 [4]), metal oxides [5,6], metal perovskite [7], and MXenes [8,9]. All aforementioned monolayers are exfoliated from their bulk lattices due to the layered structures, and they usually exhibit unconventional physical properties, distinct from their bulk counterparts.

The majority of 2D nanomaterials fabricated to date have layered structures, in which there exist weak van der Waals interlayer interaction. These weak interactions facilitate the exfoliation process and enable the possibility to derive single or few layers. The synthesis of nonlayered 2D materials, despite many challenges, not only significantly expands the field of 2D materials, but also opens new horizons in materials science. One of the first synthesized monoelemental nonlayered 2D materials was boron allotropes, borophene [10,11], which revolutionized the study of rechargeable batteries [12] and hydrogen storage [13]. The nonlayered monochalcogenides of ZnS [14] and PbS [15] were also synthesized by a bottom-up approach, exhibiting unique features for applications in solar water splitting and field-effect transistor, respectively.

Cuprous iodide, CuI, as a group 11 transition metal halide, is a nonlayered material and crystallizes in different phases [16–19]. At temperature below 370 °C, it is crystallized in cubic γ phase. In the temperature range of 370–407 °C, it is in hexagonal β phase and a transition to cubic α phase happens for higher temperatures. The bulk γ phase of CuI is known for a high thermopower coefficient and substantial optoelectric properties [20]. Very recently, ultrathin nanosheets of γ-phase CuI has been synthesized on SiO_2/Si substrate using a facile physical vapor deposition process [21]. It was also shown that the CuI nanosheets can be synthesized on the 2D substrates like WS_2 and WSe_2. Mustonen *et al.* [22] successfully synthesized monolayer CuI at ambient conditions by a single-step wet-chemical process between graphene layers. However, the mentioned articles did not provide any information on the electronic and optical properties of CuI. Indeed, no optical analysis was performed to determine the value of band gap and its type. In addition, the effect of dimensional reduction on the electronic properties of the monolayer in comparison with its bulk counterpart was not discussed.

Motivated by the recent advance on the synthesis of monolayer CuI via a novel graphene encapsulation synthesis approach, we herein investigate the electronic, excitonic,

*b92_mohebi@hotmail.com
†bohayra.mortazavi@gmail.com
‡m_bagheri@guilan.ac.ir

optical, and thermal properties of monolayer group 11 transition metal halides, including native CuI and AgI and Janus counterparts of Cu_2IBr and Ag_2IBr using first-principles calculations. The electronic and optical properties of the considered monolayers are studied using many-body perturbation calculations, and the excitonic optical properties are calculated by solving the Bethe-Salpeter equation. The dynamical and thermal stabilities of the monolayers are found to be validated by phonon dispersion spectra and *ab-initio* molecular dynamics simulations, respectively. The quasiparticle band gaps are obtained to be 4.42, 4.26, 3.93, and 3.96 eV for CuI, AgI, Cu_2BrI, and Ag_2BrI monolayers, respectively. We also examine the effects of strain and external electric field on the spin-orbit induced band splitting and find an increase of more than 100% in the magnitude of band splitting for the conduction band of Ag_2IBr under a uniaxial strain of 3%. In addition, the electric field produces a noticeable band splitting in the non-Janus monolayers. The first bright excitons of CuI, AgI, Cu_2BrI, and Ag_2BrI monolayers are found to be tightly bound with binding energies of 0.88, 0.92, 0.95, and 0.99 eV, respectively, meaning the super stability of the excitonic states against thermal decomposition at 300 K. To obtain the phonon thermal conductivity of the monolayers, the moment tensor potentials are trained over *ab-initio* molecular dynamics data sets. Then, the lattice thermal transport is evaluated using the full-iterative solution of the Boltzmann transport equation. The room-temperature thermal conductivity of CuI, AgI, Cu_2BrI, and Ag_2BrI monolayers are predicted to be remarkably low, 3.75, 2.27, 3.13, and 1.26 W/mK, respectively. Thermoelectric properties of considered monolayers are studied in the linear response regime, using Landau formalism. We find that the silver-based monolayers have a figure of merit as high as 1.4, making them promising candidates for next-generation thermoelectric devices. The presented first-principles results provide important understanding about the key physical properties of the non-Janus CuI and AgI and Janus Cu_2BrI and Ag_2BrI monolayers, which can be useful for their practical application and can guide oncoming theoretical and experimental works.

II. COMPUTATIONAL METHODS

The density functional theory (DFT) calculations are performed using the Vienna *ab-initio* simulation package (VASP) [23] on the basis of the generalized gradient approximation (GGA) and the Perdew-Burke-Ernzerhof functional for solids (PBEsol) [24]. The plane-wave and self-consistent loop energy cutoffs are set to 600 and 10^{-7} eV, respectively. The optimized lattice structures are obtained using the conjugate gradient algorithm until the Hellman-Feynman forces drop below 10^{-3} eV/Å, considering a fixed vacuum space of 20 Å along the thickness of the monolayers. The first Brillouin zone is sampled with a $15 \times 15 \times 1$ Monkhorst-Pack k-point mesh [25] based on the convergence of the total energy within 10^{-6} eV. For density of states (DOS) calculations, a denser k-point mesh of $17 \times 17 \times 1$ is used. The electronic band structure is also evaluated using the Heyd-Scuseria-Ernzerhof (HSE06) hybrid functional with the default mixing parameter ($\alpha = 0.25$) [26]. The charge transfer between atoms is determined using the Bader analysis [27].

The first-principles many-body perturbative calculations are carried out using the single-shot *GW* method [28], referred to as G_0W_0. In these calculations, the quasiparticle (QP) band gap is carefully converged with respect to the number of virtual bands, number of frequency grid points, kinetic energy cutoff, vacuum space, and k-point mesh. After the convergence tests, a set of 168, 204, 152, and 186 virtual bands is employed in the G_0W_0 calculations for CuI, AgI, Cu_2BrI, and Ag_2BrI monolayers, respectively. The number of frequency grid points is selected to be 96. The kinetic energy cutoff for the plane wave and the response function is set to be 600 and 200 eV, respectively. The vacuum space is chosen to be 30 Å and the Brillouin zone is integrated with a $9 \times 9 \times 1$ k-point mesh. See the Supplemental Material (Fig. S1 and Text S1) [29] for more details of the convergence tests. The QP band structure of the G_0W_0 calculations is interpolated using the maximally localized Wannier functions (MLWFs), as implemented in the WANNIER90 code [30]. Here the number of Wannier bands is selected to be 24 and the sp^3d^2 hybrid orbitals are chosen for the initial projections. The excitonic optical properties are studied by calculating the macroscopic dielectric function, given as $\varepsilon(\omega) = \varepsilon_1(\omega) + i\varepsilon_2(\omega)$, through solving the Bethe-Salpeter equation (BSE) [31] on top of the G_0W_0 eigenvalues. Here the Tamm-Dancoff approximation (TDA) is used, which excludes the resonant-antiresonant coupling [32]. The imaginary part of the dielectric function is obtained by summation over the empty conduction bands and the real part is transformed by the Kramers-Kronig relation, as elaborately discussed in our previous study [33]. To check the effects of self-consistency in the excitonic properties, we perform the fully self-consistent *GW* (i.e., QPGW). At this level, the QP energies and one-electron orbitals are updated four times in the calculations of the Green's function (G) and screened Coulomb interaction (W). The 15 highest occupied valence bands and the 15 lowest unoccupied conduction bands are taken into account to get a converged BSE spectrum. Unlike Ref. [34], the Hubbard term (DFT + U) [35,36] is not considered in our calculations. The reason for this choice is found in Fig. S2 and Text S2 [29].

To evaluate the phononic properties, the moment tensor potentials (MTPs) [37] are developed using the MLIP package [38]. The *ab-initio* molecular dynamics (AIMD) simulations are carried out with a time step of 1 fs and a Monkhorst-Pack k-point mesh of $2 \times 2 \times 1$ over $4 \times 3 \times 1$ supercells. Two separate AIMD calculations are conducted with the controlled temperature from 2 to 100 K and from 300 to 1000 K, each for 1000 time steps. Complete AIMD trajectories are then subsampled, and around 800 configurations are selected to train the MTPs. The phonon dispersion relations and harmonic second order interatomic force constants are obtained using the PHONOPY code [39] over $6 \times 6 \times 1$ supercells [40]. The anharmonic third order interatomic force constants are calculated using the MTPs over $6 \times 6 \times 1$ supercells [41], considering the interactions with 11th nearest neighbors. The lattice thermal transport is evaluated using the full-iterative solution of the Boltzmann transport equation (BTE) via employing the ShengBTE package [42], considering the isotope scattering.

The thermoelectric properties of the monolayers are investigated in the linear response regime using the

Landau formula. The electrical and thermal currents are defined by

$$I_E = \frac{2e}{h}\int d\epsilon T_e(\epsilon)[f_L(\epsilon) - f_R(\epsilon)], \quad (1)$$

$$I_Q = \frac{2e}{h}\int d\epsilon T_e(\epsilon)[f_L(\epsilon) - f_R(\epsilon)](\epsilon - \mu), \quad (2)$$

where $f_{L(R)}$ is the Fermi distribution function of the left (right) electrode and $T_e(\epsilon)$ denotes the electron transmission coefficient. By expanding the Fermi distribution function in terms of the chemical potential (μ) and temperature (T), the electrical conductance (G), electron thermal conductance (κ_e), and thermopower (S) are obtained by

$$G = e^2 L_0, \quad (3)$$

$$\kappa_e = \frac{1}{T}\left(L_2 - \frac{L_1^2}{L_0}\right), \quad (4)$$

$$S = \frac{\Delta V}{\Delta T}\bigg|_{I=0} = \frac{L_1}{eTL_0}, \quad (5)$$

where

$$L_n = \frac{2}{h}\int d\epsilon(\epsilon - \mu)^n T_e(\epsilon)\left(-\frac{\partial f}{\partial \epsilon}\right). \quad (6)$$

The transmission coefficient in the ballistic regime can be obtained by counting the number of bands crossing a particular energy. A dense k-point mesh of $100 \times 100 \times 1$ is used to obtain an accurate and converged transmission coefficient for each monolayer. The thermoelectric efficiency is described by figure of merit as

$$ZT = \frac{PF}{\kappa_e + \kappa_{ph}}T, \quad (7)$$

in which $PF = S^2G$ is the power factor and κ_{ph} is the lattice thermal conductance.

III. RESULTS AND DISCUSSION

A. Structural properties

After the experimental achievement by Mustonen and co-workers [22], we found CuI and AgI monolayers very interesting for exploring their physical properties. These systems belong to the group 11 transition-metal halide MX (M = Cu, Ag, Au; X = Cl, Br, I) 2D lattices, among which MCl and AuX monolayers are thermally and dynamically unstable [43]. We also constructed two Janus monolayers based on CuI and AgI native monolayers to seek fascinating properties caused by inversion symmetry breaking. For this purpose we replaced the I atoms on one side of the native monolayers with Br atoms, because with Cl atoms the stability is expected to be low. By and large, in this work, we study non-Janus CuI and AgI and Janus Cu_2BrI and Ag_2BrI monolayers, which all have highly symmetrical hexagonal lattice. Figure 1 illustrates the top and side views of CuI monolayer as a representative. Obviously the non-Janus monolayers show inversion and mirror symmetries, however, the Janus ones have only mirror symmetry. That is to say, the inversion symmetry is broken in the Janus monolayers due to the replacement of the I atom by Br atom. The relaxed lattice constant of CuI, AgI, Cu_2BrI, and Ag_2BrI monolayers according to the PBEsol functional is predicted to be 4.059, 4.402, 3.962, and 4.326 Å, respectively. Based on experimental tests [22], the distances between the Cu atomic planes and the Cu-I bond lengths along the in-plane and out-of-plane directions are 1.63 ± 0.35, 2.67 ± 0.16, and 2.55 ± 0.49 Å, respectively, which are in good agreement with the corresponding values of 1.345, 2.642, and 2.566 Å, respectively.

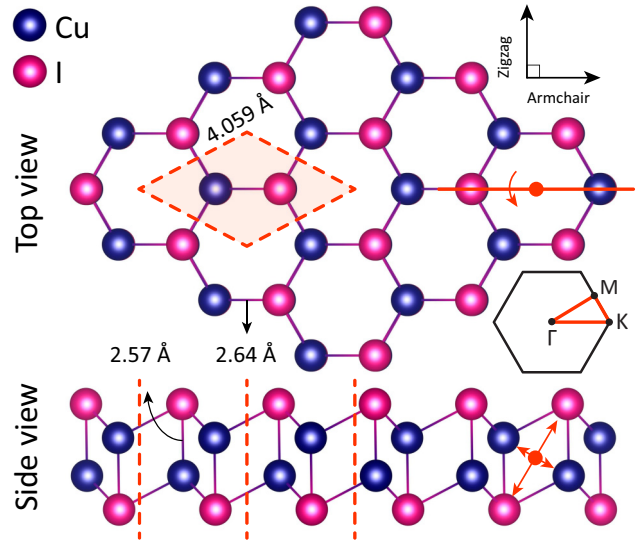

FIG. 1. Top and side views of the relaxed CuI monolayer with the first Brillouin zone. The orange dashed lines show the unit cell. The orange arrows show the mirror and inversion symmetries. The in-plane and out-of-plane Cu-I bond lengths are given.

We first study the stability of CuI, AgI, Cu_2BrI, and Ag_2BrI monolayers on the basis of the phonon dispersion relations. The obtained phonon dispersion spectra along the high symmetry points of the first Brillouin zone are depicted in Fig. S3 of the Supplemental Material [29]. Apparently there is no imaginary frequency in the phonon spectra, confirming their dynamical stability. The thermal stability of monolayers is then examined by the AIMD simulations conducted at 500 K. As shown in Fig. S4, during the simulations, the total energy of the monolayers fluctuates around the mean values, confirming their thermal stability up to 500 K. Interestingly, the C_{11} (C_{12}) elastic constant of CuI, AgI, Cu_2BrI, and Ag_2BrI monolayers is calculated to be 47 (21), 26 (15), 44 (21), and 24 (15) N/m, which reveal that these novel 2D systems are soft and include weak bonding interactions. Moreover, it is found that the systems with Cu atoms show distinctly higher rigidity than the counterparts based on Ag atoms. According to the aforementioned findings, CuI, AgI, Cu_2BrI, and Ag_2BrI monolayers are very stable but generally among soft nanomaterials.

B. Electronic and optical properties

After assuring the stability of the monolayers, we turn our attention to their electronic properties. Figure 2 displays the band structures of the monolayers together with their total and partial DOS. At the PBEsol (HSE06) level, the monolayers are semiconductors with direct band gaps of 2.10 (3.33),

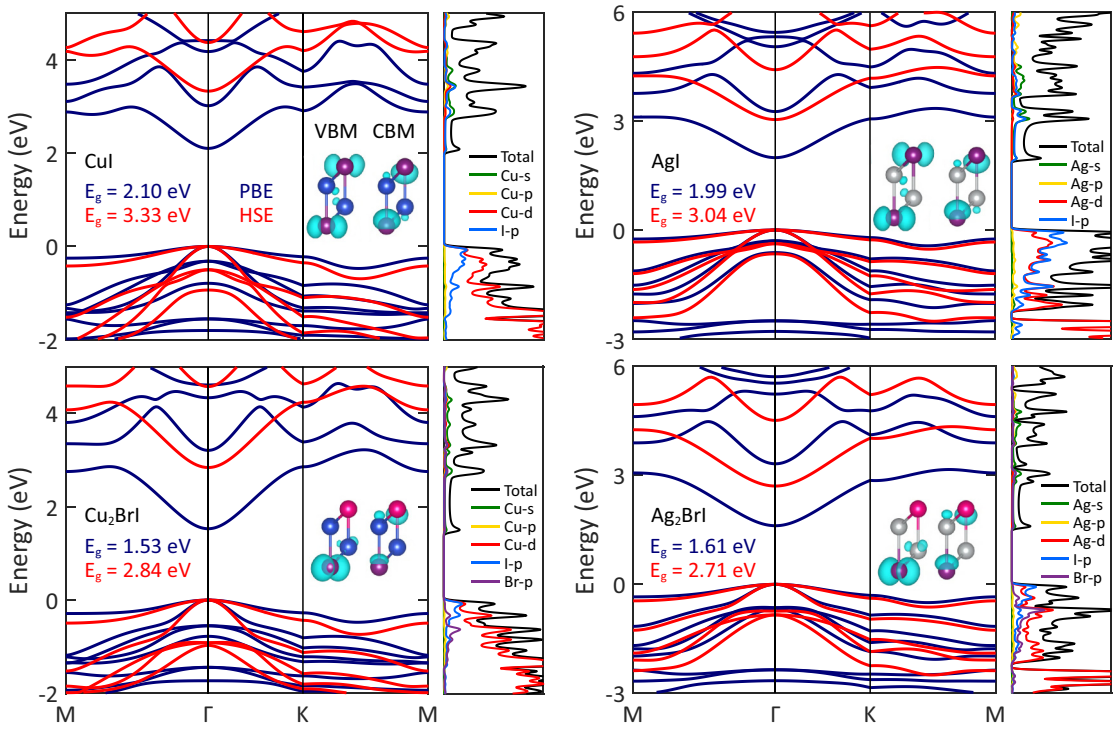

FIG. 2. Electronic band structures of the monolayers at the PBEsol (blue lines) and HSE06 (red lines) levels along with the DOS at the PBEsol level. The VBMs are set to zero. The squares of the wave functions at the VBM and CBM are shown in the insets.

1.99 (3.04), 1.53 (2.84), and 1.61 (2.71) eV for CuI, AgI, Cu_2BrI, and Ag_2BrI, respectively. Except for the band gaps, the characteristics of the band structures are the same at both levels. That is to say, including a fraction (0.25) of the exact Hartree-Fock exchange energy in the DFT formulation only corrects the band gaps by 1.23, 1.05, 1.31, and 1.10 eV for CuI, AgI, Cu_2BrI, and Ag_2BrI, respectively. For all the monolayers, the valence band maximum (VBM) and the conduction band minimum (CBM) are located at the Γ point. The conduction band edges are quadratically dispersed, which show free electrons. The valence band edges are nearly flat, which represent localized holes. Although the valence bands edges at the Γ point show double degeneracy, there is a tiny gap of 10^{-3} eV between the heavy and light hole subbands. It is worth noting that the band gaps calculated for CuI and AgI monolayers agree very well with those reported in a previous study [43].

From the DOS, it is seen that the CBMs are equally contributed by the *s* orbitals of the Cu/Ag atoms and the *p* orbitals of the Br/I atoms while the VBMs are mostly controlled by the *d* orbitals of the Cu/Ag atoms and the *p* orbitals of the I atoms. Therefore, the optical selection rules allow the transitions between the *p* orbitals of the halogen atoms and the *s* orbitals of the transition metal ones. No considerable participation from Br atoms is found near the edge of a valence band while contributing the most at the edge of a conduction band in the Janus monolayers, which is in line with the reduction of the band gap by substituting Br atoms. The shapes of the wave functions at the VBMs and CBMs support the above discussion. As shown in the insets of Fig. 2, at the VBMs of the non-Janus monolayers, the wave functions are shaped like dumbbells, which are distributed along the *x* direction and centered on the I atoms, showing the p_x orbitals of the I atoms. At the CBMs, the wave functions are formed spherically on the Cu/Ag atoms and hemispherically on the I atoms, referred to as *s* and p_z orbitals, respectively. For Ag_2BrI and Cu_2BrI Janus monolayers, the wave functions of the VBMs exhibit a hybridization between the p_x and p_y orbitals of the I atoms. At the CBMs, one can see the predominant contribution of the p_z orbitals of the halogen atoms. The charge density difference (CDD) isosurface of the monolayers is depicted in Fig. 3, where the yellow and cyan colors denote the charge accumulation and depletion, respectively. Apparently the highest charge accumulation is located at the center of the atomic bonds, indicating the covalent bonding characteristics. The highest charge depletion is around the transition metal atoms. In accordance with the CDD analysis, for CuI structure, we find that $0.273e$ is transferred from the Cu to I atoms. While for AgI structure, $0.237e$ is transported from the Ag to I atoms. These are in line with the larger electronegativity of the I (2.66) atom compared to the Cu (1.90) and Ag (1.93) transition metals. In Cu_2BrI Janus monolayer, the charge transfer from the two neighboring Cu atoms to the uppermost and lowermost layers of the halogen atoms is different. That is to say, the Br atoms receive more charge compared to the I atoms due to the larger electronegativity of the Br (2.96) atom. Also, in Ag_2BrI Janus monolayer, the two neighboring Ag atoms lose different amounts of charge in such a manner that 65% of the total transferred charge is delivered to the Br atoms and the rest is sent to the I atoms. These differences result in a potential gradient normal to the basal plane, forming an electric field between the uppermost and lowermost layers. The intrinsic out-of-plane electric field caused by the inversion symmetry breaking in Janus monolayers leads to spin-valley

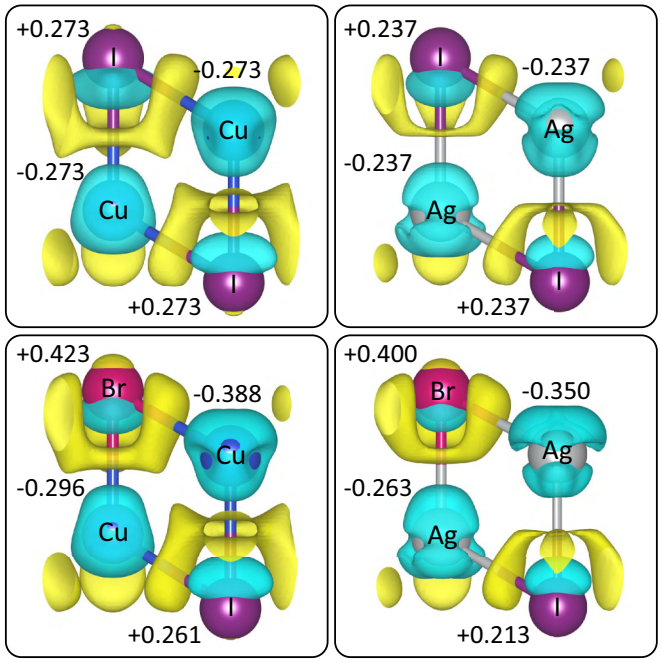

FIG. 3. Charge density difference of the monolayers with the Bader charge transfer between atoms. The isosurface of charge accumulation and depletion was set to $5 \times 10^{-3} e/\text{bohr}^3$.

splitting and Rashba spin splitting when combined with spin-orbit coupling (SOC) and magnetic proximity effect [44–46].

We check out the effects of SOC in the band structures. By including SOC at the PBEsol (HSE06) level, the numbers of energy bands are doubled and the band gaps are reduced to 1.86 (3.03), 1.72 (2.73), 1.31 (2.58), and 1.37 (2.44) eV for CuI, AgI, Cu_2BrI, and Ag_2BrI monolayers, respectively. As shown in Fig. S5 (Fig. S6), for CuI and AgI monolayers, SOC cannot remove the double degeneracy of the individual energy states while for the Janus monolayers, the bands are split. This spin splitting, referred to as Zeeman-type splitting, is in fact a consequence of SOC combined with inversion symmetry breaking. At the PBEsol level, the spin splitting constant at the Γ point is zero but at the K point, the spin splitting of valence (conduction) band edge is 12 (28) and 13 (45) meV for Cu_2BrI and Ag_2BrI monolayers, respectively. The SOC also increases the tiny gap observed between the heavy and light hole subbands at the Γ point up to 400 and 450 meV for the non-Janus and Janus monolayers, respectively. At the HSE06 level, the strength of SOC is predicted to be higher. Hence, the reported values for spin splitting will be slightly larger at this level. By and large, one can conclude that the main effect of SOC is on the valence bands owing to the hybridization between the d orbitals of the Cu/Ag atoms and the p orbitals of the I atoms. The conduction bands are not influenced by SOC due to the predominant participation of the s orbitals of the Cu/Ag atoms.

In experimental syntheses, 2D materials are grown on different kinds of substrates. These substrates can affect the intrinsic properties of 2D materials. The most common effect of the substrate is applying strain to the overlayer. If the substrate is active, the interactions between the substrate and 2D material can strongly affect the electronic properties of the overlayer. In this part we examine the dependence of spin-orbit induced band splitting on the applied strain. It should be noted that strain is only applied in the form of uniaxial in the armchair and zigzag directions because it can break the inversion symmetry of materials. The combination of SOC and inversion symmetry breaking produces attractive effects such as Rashba [47] and valleytronic [48]. Inversion symmetry is inherently broken in Janus structures, and as noted, SOC causes band splitting at the K points. The maximum band splitting in Cu_2BrI and Ag_2BrI Janus monolayers as a function of strain is plotted in Fig. 4(a). Irrespective of direction, strain slightly reduces the valence band splitting. In contrast, we see an increase in the conduction band splitting with strain. The stronger spin splitting in the conduction band is due to the predominant role of the transition metal atom in the conduction band, which is observable from the DOS. The rate of increase for strain in the armchair direction is slightly higher than that in the zigzag direction. The increase in Ag_2BrI structure is much more intense than in Cu_2BrI monolayer. A strain of about 1%–3% in Ag_2BrI monolayer can cause an increase of more than 100% in the magnitude of conduction band splitting. Strong SOC interactions, inherent electric field, and increased inversion symmetry breaking by strain are the main reasons for the observed increase.

We additionally examine the spin-orbit induced band splitting of CuI and AgI monolayers. Interestingly, although strain can slightly alter the symmetries of the structures, no band splitting induced by SOC is observed in these monolayers. The softness of the materials, which was also confirmed in experimental reports [22], is a major obstacle for engineering the band structures and creating the Zeeman-type or Rashba-type spin splitting with strain. Our evaluation shows that applying strain is not a good approach for tuning the properties of CuI and AgI monolayers. Hence, they can be grown on substrates with different lattice constants while showing the same electronic properties.

Figure 4(b) illustrates the variations of the band gaps of Cu_2BrI and Ag_2BrI Janus monolayers as a function of strain. Apparently an increase of 20% (10%) is observed in the band gap of Ag_2BrI monolayer under the strain of 5% in the armchair (zigzag) direction. This is attributed to the presence of a heavy transition metal such as silver and the absence of an inversion symmetry center in this Janus monolayer, which are critical for the noticeable change in the band gap. The variation of the band gap in Ag_2BrI monolayer is much more intense than that in Cu_2BrI, which is in line with the smaller elastic constants of Ag_2BrI monolayer. In other structures, the changes in band gaps under strain up to 5% are less than 3% (see Fig. S8).

We also explore the spin-orbit induced band splitting in the presence of an external electric field. In contrast to strain, the electric field produces a noticeable band splitting in CuI and AgI monolayers. The splitting is visible throughout the Brillouin zone, as shown in Figs. 4(c) and S7. For AgI (CuI) monolayer, the largest valence band splitting occurs in the K-M path and can reach 140 (73) meV under an electric field of 0.5 eV/Å, which is comparable to transition metal dichalcogenide monolayers. The largest conduction band splitting occurs at the K point. Also, a Rashba-type band

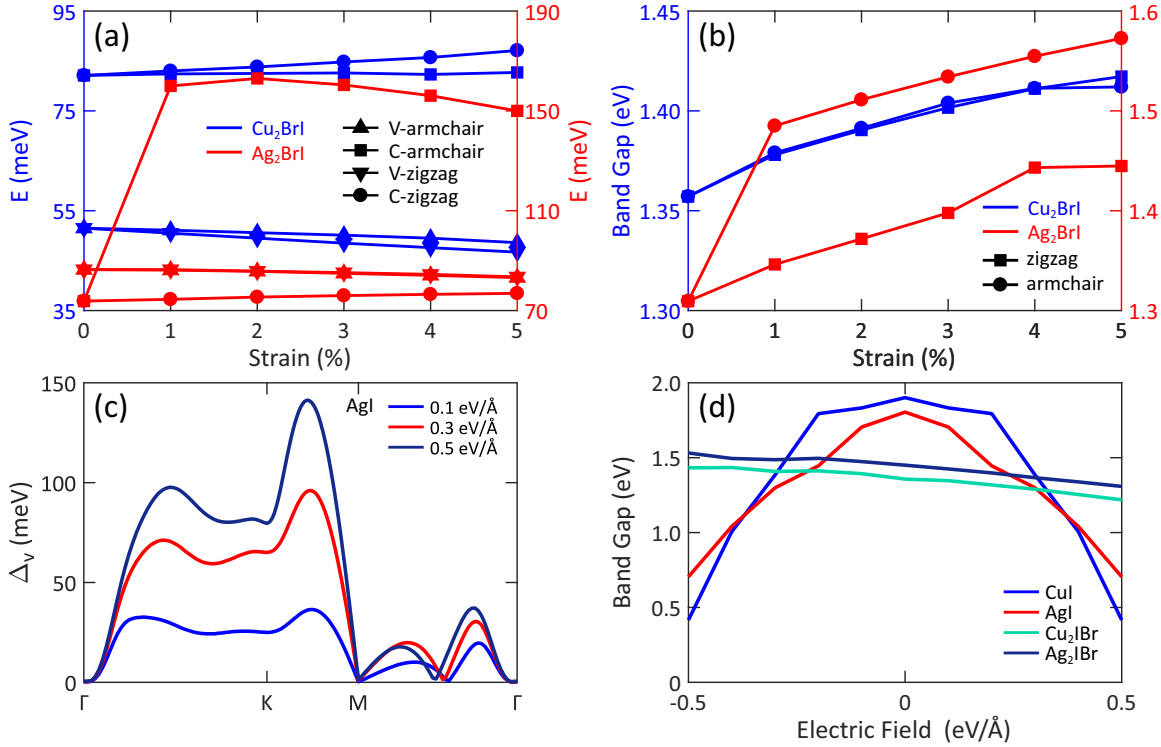

FIG. 4. (a) Spin-orbit induced valence and conduction bands splitting and (b) band gap variation of Cu_2BrI and Ag_2BrI Janus monolayers as a function of uniaxial strain along the armchair and zigzag directions. (c) Spin-orbit induced valence band splitting of AgI monolayer under different electric fields. The rest of the results are available in Fig. S7. (d) Band gap variation of the monolayers as a function of electric field.

splitting is observed in the Γ-K path under strong electric fields. Comparing the band splitting in CuI and AgI monolayers shows that it is directly related to the transition metal atoms. The larger the atomic number is, the greater the band splitting will be. However, in the Janus structures, the dependence of band splitting on the electric field is very weak as shown in Fig. S7. Due to the lack of an inversion center, there is an inherent electric field in these structures that leads to a noticeable band splitting. Therefore, the external electric field cannot significantly change the band splitting. Interestingly, unlike the non-Janus structures, increasing the strength of the external field has no effect on the magnitude of band splitting. Also, the direction of electric field does not have a significant effect on the results.

The variation of the band gaps as a function of external electric field is shown in Fig. 4(d). In CuI and AgI non-Janus monolayers, due to the inversion symmetry and the arrangement of atoms in the lower and upper planes, the changes in the band gaps are independent of the direction of electric field. By increasing the intensity of electric field, the band gaps decrease and the reduction is more for CuI monolayer. On the contrary, in the Janus structures, the changes in the band gaps in addition to the magnitude of electric field depend on its direction. A linear increase is observed in the band gaps with the electric field in the $-z$ direction. While we see a decrease in the band gaps by increasing the electric field in the $+z$ direction. The band gaps reduction directly depends on the difference in charge transferred between two halogen atoms. As the electric field increases in the $+z$ direction, we observe more charge transfer towards the Br atoms, which reduces the band gaps. In contrast, the external electric field in the $-z$ direction is in the opposite direction of the intrinsic electric field caused by the dipole inside the monolayers, which reduces the difference in the charge accumulated on halogen atoms, giving rise to the band gaps.

To capture the role of electron-electron exchange interaction in the electronic structure, we step beyond the PBEsol and HSE06 levels using the non-self-consistent *GW* approach, known as G_0W_0. The G_0W_0 band structure of the monolayers in the absence of SOC interaction is available in Fig. S9. As can be noticed, the general shapes of the band structures are similar to those calculated with the PBEsol functional. All the monolayers still have direct band gaps at the Γ point. However, the values of band gaps are different from the PBEsol calculations due to the self-energy corrections. At this level, the QP band gaps are obtained to be 4.42, 4.26, 3.93, and 3.96 eV for CuI, AgI, Cu_2BrI, and Ag_2BrI monolayers, respectively. Such large self-energy corrections of 2.32, 2.27, 2.40, and 2.35 eV emphasize the importance of electron-electron interaction in these structures. Also, it is found that increasing the atomic weight of the halogen (transition metal) atom increases (decreases) the QP band gap of the monolayer. Owing to the deformation of the bands dispersion, a rigid shift of the conduction bands with respect to the VBMs does not describe the self-energy effects properly. Including SOC reduces the QP band gaps down to 4.02, 3.85, 3.59, and 3.61 eV for CuI, AgI, Cu_2BrI, and Ag_2BrI monolayers, respectively. As expected, the structure with heavier atoms has the strongest SOC. To better compare, we listed the band gaps calculated at different levels in Table I.

TABLE I. Band gaps calculated for the considered monolayers at different levels of theory in the unit of eV.

Structure	PBEsol	PBEsol + SOC	HSE06	HSE06+SOC	G_0W_0	G_0W_0 + SOC	Optical
CuI	2.10	1.86	3.33	3.03	4.42	4.02	3.14
AgI	1.99	1.72	3.04	2.73	4.26	3.85	2.93
Cu_2BrI	1.53	1.31	2.84	2.58	3.93	3.59	2.64
Ag_2BrI	1.61	1.37	2.71	2.44	3.96	3.61	2.62

We study the excitonic optical properties of the monolayers by solving the Bethe-Salpeter equation over the G_0W_0 eigenvalues (i.e., G_0W_0 + BSE), which includes electron-electron and electron-hole interactions. These interactions have been shown to play a vital role in the optical properties of 2D materials [49,50]. To clarify the role of the many-body effects, we also calculated the optical spectra of the monolayers using the random-phase approximation (RPA) over the G_0W_0 (i.e., G_0W_0 + RPA) and DFT (i.e., DFT + RPA), where the aforementioned interactions are excluded. Owing to the symmetric and isotropic crystal structure of the monolayers, the optical coefficients along the x direction ($E \parallel x$) are identical to those along the y direction ($E \parallel y$). On the other hand, due to the strong depolarization effect in 2D systems for polarization perpendicular to the plane ($E \parallel z$), the optical coefficients along the z direction are negligible. Therefore, we only study the optical response of the monolayers for x-polarized light. Figure 5 illustrates the imaginary part of the dielectric function of the monolayers at three different levels of theory for light polarized along the x direction. As it is obvious, at the DFT + RPA level, the optical spectra of the monolayers show numerous peaks, which are associated with the doubling of bands in the presence of SOC interaction. At this level, the first peak appears at 1.85, 1.71, 1.30, and 1.36 eV for CuI, AgI, Cu_2BrI, and Ag_2BrI monolayers, respectively. These peaks correspond to direct transitions from the highest valence band to the lowest conduction band at the Γ point. Including electron-electron interaction (i.e., G_0W_0 + RPA) results in a blueshift in the optical spectra and reduces the intensity of the peaks overestimated by the DFT + RPA level. The electron-electron interaction also decreases the number of peaks. On the other hand, considering electron-hole interaction leads to a cancellation effect and subsequently a redshift in the optical spectra. The electron-hole interaction modifies the general shape of the spectra. At this level (i.e., G_0W_0 + BSE), the first peaks, referred to as optical gaps, appear at 3.14, 2.93, 2.64, and 2.62 eV, which correspond to tightly bound excitons with binding energies of 0.88, 0.92, 0.95, and 0.99 eV for CuI, AgI, Cu_2BrI, and Ag_2BrI monolayers, respectively. This is very interesting because in 2D materials the binding energy of the first bright exciton is directly proportional to the band gap [51,52]. Basically, the smaller the QP band gap is, the

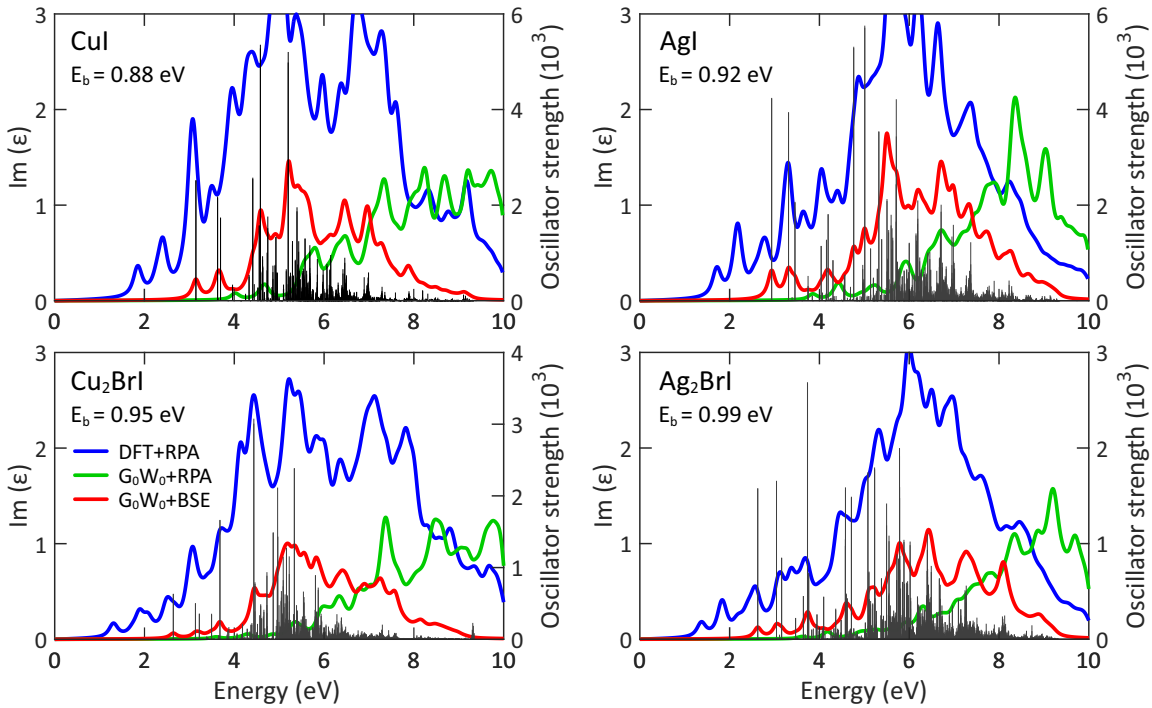

FIG. 5. Imaginary part of the dielectric function of the monolayers at different levels of theory including the DFT + RPA (electron-electron and electron-hole interactions excluded), G_0W_0 + RPA (electron-electron interaction included and electron-hole interaction excluded), and G_0W_0 + BSE (electron-electron and electron-hole interactions included) together with the optical oscillator strength. The exciton binding energy (E_b), the difference between the G_0W_0 + SOC band gap and the optical gap, is given for each monolayer.

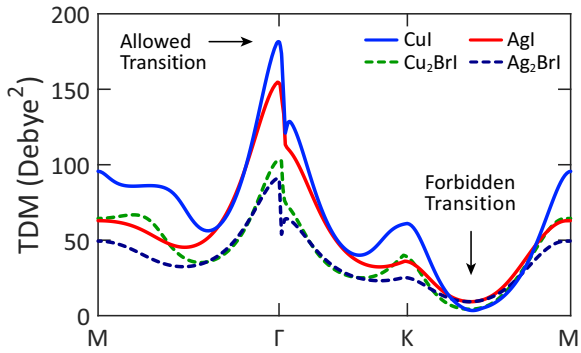

FIG. 6. Amplitude of TDM for the considered monolayers along the high symmetry points of the Brillouin zone.

stronger the Coulomb screening becomes. Stronger Coulomb screening naturally results in a smaller exciton binding energy and a larger exciton Bohr radius. However, our results show that the substitution of the Br atoms reduces the QP band gap of the monolayer and increases the exciton binding energy. This is probably because the intrinsic electric field caused by inversion symmetry breaking reduces the Coulomb screening, leading to a larger exciton binding energy. The calculated binding energy for each monolayer indicates the first bright exciton to be strongly confined in an area with a Bohr radius smaller than the bond length, referring to as Frenkel-type exciton, meaning the superstability of the excitonic states against thermal decomposition. The obtained optical gaps reveal the potential application of the monolayers in the ultraviolet region. The optical oscillator strength of the monolayers is also depicted in Fig. 5. Oscillator strength is a dimensionless quantity that expresses the probability of absorption or emission of electromagnetic radiation in transitions between the energy levels. Hence, bright transitions will have large oscillator strengths. As can be seen, there are many excitonic states with large oscillator strengths. For instance, the oscillator strength of the first peak is 2519, 4243, 634, and 1578 for CuI, AgI, Cu_2BrI, and Ag_2BrI monolayers, respectively. This means that the first peak of the optical spectra corresponds to a bright exciton. On the contrary, we have many dark transitions with small oscillator strength, which are known as spin-forbidden dark excitons. Among the most important ones, one can refer to the spin-forbidden dark exciton below the optical gap at 3.13, 2.92, 2.63, and 2.61 eV for CuI, AgI, Cu_2BrI, and Ag_2BrI monolayers, respectively. These excitons have lower energy ($\sim$0.01 eV) than the first bright exciton. Therefore, the ground state exciton of these monolayers are dark.

Figure 6 provides the amplitude of transition dipole moment (TDM) of the monolayers from the highest occupied valence band to the lowest unoccupied conduction band. TDM is a complex vector quantity that includes the phase factors associated with the two states, and the amplitude of TDM gives the probability of transition between the two states. Obviously, for all the monolayers, the amplitude of TDM is very small in the $K \rightarrow M$ path, implying no optical absorption between the two states in this path. Meanwhile, the largest amplitude is located at the Γ point, revealing the high probability of transition between the VBM and CBM. The transition at the Γ point is known as allowed transition.

Owing to the dependence of the single-shot G_0W_0 method on the DFT mean-field starting points, we performed the fully self-consistent *GW* calculation for CuI monolayer. As shown in Fig. S10, updating the eigenvalues and eigenstates leads to a slight redshift in the imaginary part of the dielectric function. Also, the intensity of peaks is reduced while the location and the number of peaks remain almost unchanged. As a result, the binding energy of the ground state exciton is obtained to be 0.87 eV, very close to that achieved from the G_0W_0 + BSE calculation. By and large we find that the obtained results are not dependent on the choice of input parameters.

The other optical coefficients of the monolayers, i.e., the real part of the dielectric function, absorption coefficient, and reflectivity are calculated at the G_0W_0 + BSE level. As shown in Fig. S11(a), the static dielectric constant of the monolayers is 1.36, 1.44, 1.29, and 1.32 for CuI, AgI, Cu_2BrI, and Ag_2BrI monolayers, respectively. That is to say, with increasing the average atomic number of the monolayer, the static dielectric constant increases. It is also seen that the real part of the dielectric function remains always positive in the entire range, showing the ultralow reflectivity of the monolayers. From the absorption coefficients, it is understood that the monolayers are good absorbers in the ultraviolet region (3.26 to 10 eV). The mean value of absorption in this region is 1.37, 1.87, 1.16, and 1.44×10^7 m^{-1} for CuI, AgI, Cu_2BrI, and Ag_2BrI monolayers, respectively. Indeed, the structure with the largest (smallest) atomic number has the largest (smallest) absorption rate. From Fig. S11(c) it can be seen that the monolayers are highly transparent in the visible light region (1.63 to 3.26 eV). In addition, the mean value of reflectivity in the entire region remains under 3%, 4%, 2%, and 2% for CuI, AgI, Cu_2BrI, and Ag_2BrI monolayers, respectively. Overall, for their band gaps, ultrahigh transparency, and flexibility, the monolayers are predicted to be very suitable for application as electron and hole transport layers in a solar cell.

C. Thermoelectric properties

We now investigate the temperature-dependent lattice thermal conductivity of CuI, AgI, Cu_2BrI, and Ag_2BrI monolayers, as it is illustrated in Fig. 7. The results show isotropic lattice thermal conductivity in these novel monolayers, which is consistent with their highly symmetrical lattice. At 300 K, the thermal conductivity of CuI, AgI, Cu_2BrI, and Ag_2BrI monolayers taking the isotope scattering into account are predicted to be remarkably low as 3.75, 2.27, 3.13, and 1.26 W/mK, respectively. We found that the lattice thermal conductivity in these systems follows the T^{-1} trend with respect to the temperature (T). The predicted values for thermal conductivity are also consistent with the classical theory saying a material with lower elastic modulus and higher atomic weight shows lower thermal conductivity. By increasing temperature up to 800 K, due to the enhanced phonon scattering, the thermal conductivity of CuI, AgI, Cu_2BrI, and Ag_2BrI monolayers are reduced to 1.40, 0.85, 1.16, and 0.47 W/mK, which are very promising for thermoelectric applications.

To better understand the underlying mechanism resulting in the low lattice thermal conductivity of these novel 2D

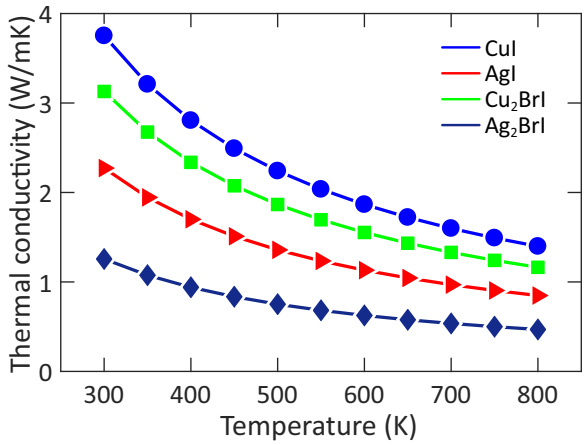

FIG. 7. Lattice thermal conductivity of the monolayers as a function of temperature considering the isotope scattering.

materials, in Fig. 8 we compare their phonon group velocity and lifetime. As expected, with the weakening of the atomic bonds, the phonon group velocities are considerably suppressed in the AgI monolayer, which is more noticeable for low-frequency acoustic modes. This is consistent with the observed narrower dispersions for the acoustic phonon modes in AgI monolayer than those of CuI and Cu_2BrI counterparts. The phonon lifetime for these systems shows closer trends. It is noticeable that while the phonon group velocities are close for CuI and Cu_2BrI monolayers, the phonon lifetime is generally lower, particularly between 1–4 THz, in Cu_2BrI monolayer than corresponding modes in the CuI counterpart, explaining its lower thermal conductivity.

The transmission coefficient of the considered monolayers is plotted in Fig. S12. As discussed in previous sections, with increasing (decreasing) the atomic weight of the transition metal (halogen) atom, the band gap is reduced, which is consistent with transmission spectrum. The transmission coefficient has larger values in negative energies that is consistent with the band structure. Above the Fermi level we see a gap between the bands while the density of the bands below the Fermi level is high and many degeneracies are evident. This band pattern is visible in the transmission coefficient. Therefore, the electronic and thermoelectric properties of these materials with *p*-type doping are expected to be much better than *n*-type doping. The thermopower and PF of the monolayers are plotted in Fig. S13. Negative (positive) values of chemical potential indicate *p* (*n*)-type doping. As it is clear, the thermopower increases with decreasing the atomic mass of the transition metal, which is due to the increase of the band gap. The thermopower has the highest value near the Fermi level, and decreases rapidly at energies away from the Fermi level because of bipolar effect. Another point about the thermopower is its inverse dependence on temperature. As shown in Fig. S14, the thermopower decreases significantly with increasing temperature. The thermopower of CuI and AgI monolayers is about 4 mV/K, which is higher than $ZnIn_2X_4$ (X = S, Se, Te) [53], WSX (X = S, Se, Te) [54] and phosphorene [55].

As expected from the discussion above, the magnitude of PF in *p*-type doping is significantly higher than that in *n* type. This is attributed to the degeneracy of the bands below the Fermi level and the asymmetry of the electrical conductance. The electrical conductance of monolayers in *p*-type doping is more than 5 times larger than that in *n* type, as shown in Fig. S15. In negative energies away from the Fermi level, the PF in Janus structures is higher than that in non-Janus samples, which is directly related to the electrical conductance. The electrical conductance of Janus monolayers exhibits nonlinear behavior in *p*-type doping. Unlike thermopower, PF increases significantly with temperature (see Fig. S16). This increase is due to remarkable changes in the electrical conductance with temperature.

The ZT of the monolayers as a function of chemical potential and temperature is plotted in Fig. 9. The results show the presence of two dominant peaks on both sides of the Fermi level, which agrees very well with PF. With increasing the temperature, the peaks are widened, which is due to the significant increase of electronic conductivity and decrease of lattice thermal conductivity with temperature. The magnitude of ZT in *p*-type doping is much higher than that in *n* type. In

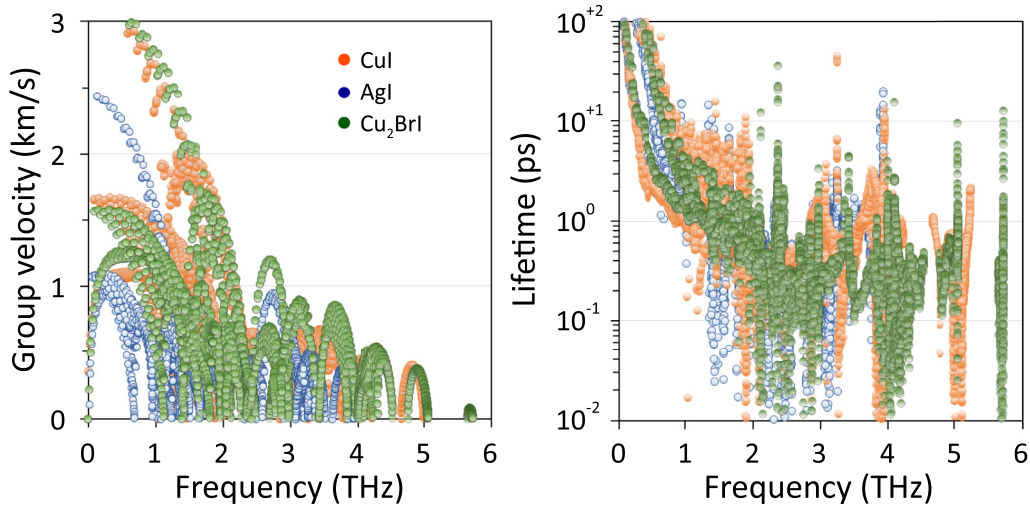

FIG. 8. Frequency dependent phonon group velocity and lifetime of the monolayers at 300 K.

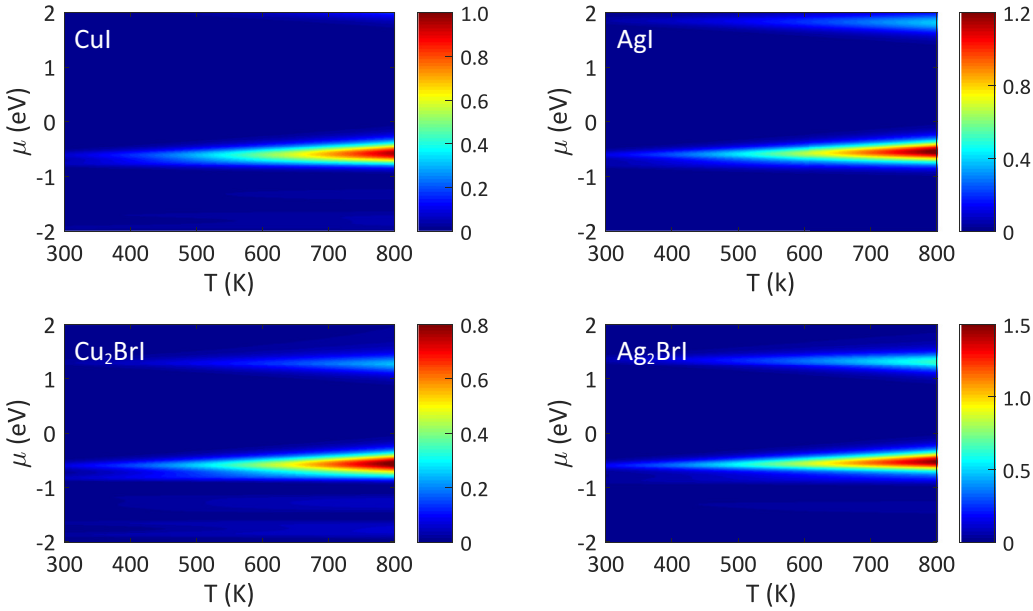

FIG. 9. Thermoelectric figure of merit of the monolayers as a function of chemical potential and temperature.

addition, ZT is larger in Ag structures than Cu ones, which is directly related to the smaller lattice thermal conductivity in these structures, as can be seen in Fig. 7.

IV. CONCLUSION

Motivated by the successful synthesis of novel CuI and AgI monolayers via the graphene encapsulation approach, herein, we carried out elaborated first-principles simulations to explore the key physical properties of non-Janus CuI and AgI and Janus Cu_2BrI and Ag_2BrI monolayers. We found that these novel 2D systems are stable, but are also soft materials with low elastic modulus. On the basis of the full-iterative solution of the Boltzmann transport equation, the lattice thermal conductivity of CuI, AgI, Cu_2BrI, and Ag_2BrI monolayers at room temperature were predicted to be remarkably low, 3.75, 2.27, 3.13, and 1.26 W/mK, respectively, which are promising for thermoelectric applications. The electronic and optical properties were explored using many-body perturbation calculations. Particularly, the excitonic effects on the optical properties were taken into account by solving the Bethe-Salpeter equation. The optical gaps were obtained to be 3.14, 2.93, 2.64, and 2.62 eV for CuI, AgI, Cu_2BrI, and Ag_2BrI monolayers, which correspond to tightly bound excitons with binding energies of 0.88, 0.92, 0.95, and 0.99 eV, respectively. Effects of mechanical straining and electric filed on the tenability of the electronic and optical properties were also analyzed. The thermopower of considered monolayers is higher than 3000 μV/K at room temperature, indicating their high thermoelectric efficiency. The presented results provide an important and extensive vision for the key physical properties of the non-Janus CuI and AgI and Janus Cu_2BrI and Ag_2BrI monolayers and can be valuable to the future applications of optoelectronic devices.

ACKNOWLEDGMENTS

B.M. and X.Z. appreciate the funding by the Deutsche Forschungsgemeinschaft (DFG, German Research Foundation) under Germany's Excellence Strategy within the Cluster of Excellence PhoenixD (EXC 2122, Project ID 390833453). B.M. is greatly thankful to the VEGAS cluster at the Bauhaus University of Weimar for providing the computational resources.

The authors declare that they have no conflict of interest.

[1] Q. Bao and K. P. Loh, ACS Nano **6**, 3677 (2012).
[2] H. Zeng, J. Dai, W. Yao, D. Xiao, and X. Cui, Nat. Nanotechnol. **7**, 490 (2012).
[3] H. R. Gutierrez, N. Perea-Lopez, A. L. Elias, A. Berkdemir, B. Wang, R. Lv, F. Lopez-Urias, V. H. Crespi, H. Terrones, and M. Terrones, Nano Lett. **13**, 3447 (2013).
[4] H. Fang, S. Chuang, T. C. Chang, K. Takei, T. Takahashi, and A. Javey, Nano Lett. **12**, 3788 (2012).
[5] B. Y. Zhang, K. Xu, Q. Yao, A. Jannat, G. Ren, M. R. Field, X. Wen, C. Zhou, A. Zavabeti, and J. Z. Ou, Nat. Mater. **20**, 1073 (2021).
[6] H.-J. Liu, J.-C. Lin, Y.-W. Fang, J.-C. Wang, B.-C. Huang, X. Gao, R. Huang, P. R. Dean, P. D. Hatton, Y.-Y. Chin *et al.*, Adv. Mater. **28**, 9142 (2016).
[7] D. Ji, S. Cai, T. R. Paudel, H. Sun, C. Zhang, L. Han, Y. Wei, Y. Zang, M. Gu, Y. Zhang *et al.*, Nature (London) **570**, 87 (2019).
[8] Y. Gogotsi and B. Anasori, ACS Nano **13**, 8491 (2019).
[9] M. Naguib, M. W. Barsoum, and Y. Gogotsi, Adv. Mater. **33**, 2103393 (2021).
[10] A. J. Mannix, X.-F. Zhou, B. Kiraly, J. D. Wood, D. Alducin, B. D. Myers, X. Liu, B. L. Fisher, U. Santiago, J. R. Guest *et al.*, Science **350**, 1513 (2015).

[11] A. J. Mannix, Z. Zhang, N. P. Guisinger, B. I. Yakobson, and M. C. Hersam, Nat. Nanotechnol. **13**, 444 (2018).

[12] X. Zhang, J. Hu, Y. Cheng, H. Y. Yang, Y. Yao, and S. A. Yang, Nanoscale **8**, 15340 (2016).

[13] J. Joseph, V. S. Sivasankarapillai, S. Nikazar, M. S. Shanawaz, A. Rahdar, H. Lin, and G. Z. Kyzas, ChemSusChem **13**, 3754 (2020).

[14] Y. Sun, Z. Sun, S. Gao, H. Cheng, Q. Liu, J. Piao, T. Yao, C. Wu, S. Hu, S. Wei *et al.*, Nat. Commun. **3**, 1057 (2012).

[15] S. Acharya, B. Das, U. Thupakula, K. Ariga, D. Sarma, J. Israelachvili, and Y. Golan, Nano Lett. **13**, 409 (2013).

[16] S. Miyake, S. Hoshino, and T. Takenaka, J. Phys. Soc. Jpn. **7**, 19 (1952).

[17] P. M. Sirimanne, T. Soga, and M. Kunst, J. Solid State Chem. **178**, 3010 (2005).

[18] P. Luhanga, C. Muiva, S. Coetzee, K. Maabong, L. Tiedt, and P. Monowe, J. Optoelectron. Adv. Mater. **18**, 837 (2016).

[19] D. Chen, Y. Wang, Z. Lin, J. Huang, X. Chen, D. Pan, and F. Huang, Cryst. Growth Des. **10**, 2057 (2010).

[20] M. Grundmann, F.-L. Schein, M. Lorenz, T. Böntgen, J. Lenzner, and H. von Wenckstern, Phys. Status Solidi (a) **210**, 1671 (2013).

[21] K. Yao, P. Chen, Z. Zhang, J. Li, R. Ai, H. Ma, B. Zhao, G. Sun, R. Wu, X. Tang *et al.*, npj 2D Mater. Appl. **2**, 16 (2018).

[22] K. Mustonen, C. Hofer, P. Kotrusz, A. Markevich, M. Hulman, C. Mangler, T. Susi, T. J. Pennycook, K. Hricovini, C. Richter *et al.*, Adv. Mater. **34**, 2106922 (2022).

[23] G. Kresse and J. Furthmüller, Phys. Rev. B **54**, 11169 (1996).

[24] G. I. Csonka, J. P. Perdew, A. Ruzsinszky, P. H. T. Philipsen, S. Lebègue, J. Paier, O. A. Vydrov, and J. G. Ángyán, Phys. Rev. B **79**, 155107 (2009).

[25] H. J. Monkhorst and J. D. Pack, Phys. Rev. B **13**, 5188 (1976).

[26] A. V. Krukau, O. A. Vydrov, A. F. Izmaylov, and G. E. Scuseria, J. Chem. Phys. **125**, 224106 (2006).

[27] G. Henkelman, A. Arnaldsson, and H. Jónsson, Comput. Mater. Sci. **36**, 354 (2006).

[28] M. Shishkin and G. Kresse, Phys. Rev. B **75**, 235102 (2007).

[29] See Supplemental Material at http://link.aps.org/supplemental/10.1103/PhysRevB.106.125405 for phonon dispersion spectra, AIMD simulations, and quasiparticle G_0W_0 levels. Optical coefficients and thermoelectric coefficients are also presented.

[30] A. A. Mostofi, J. R. Yates, G. Pizzi, Y.-S. Lee, I. Souza, D. Vanderbilt, and N. Marzari, Comput. Phys. Commun. **185**, 2309 (2014).

[31] M. Rohlfing and S. G. Louie, Phys. Rev. B **62**, 4927 (2000).

[32] G. Onida, L. Reining, and A. Rubio, Rev. Mod. Phys. **74**, 601 (2002).

[33] M. A. Mohebpour, S. M. Mozvashi, S. I. Vishkayi, and M. B. Tagani, Phys. Rev. Materials **6**, 014012 (2022).

[34] W. Gao, W. Xia, Y. Wu, W. Ren, X. Gao, and P. Zhang, Phys. Rev. B **98**, 045108 (2018).

[35] M. Fronzi, M. H. N. Assadi, and D. A. Hanaor, Appl. Surf. Sci. **478**, 68 (2019).

[36] S. L. Dudarev, G. A. Botton, S. Y. Savrasov, C. J. Humphreys, and A. P. Sutton, Phys. Rev. B **57**, 1505 (1998).

[37] A. V. Shapeev, Multiscale Model. Simul. **14**, 1153 (2016).

[38] I. S. Novikov, K. Gubaev, E. V. Podryabinkin, and A. V. Shapeev, Mach. Learn.: Sci. Technol. **2**, 025002 (2020).

[39] A. Togo and I. Tanaka, Scr. Mater. **108**, 1 (2015).

[40] B. Mortazavi, I. S. Novikov, E. V. Podryabinkin, S. Roche, T. Rabczuk, A. V. Shapeev, and X. Zhuang, Appl. Mater. Today **20**, 100685 (2020).

[41] B. Mortazavi, E. V. Podryabinkin, I. S. Novikov, T. Rabczuk, X. Zhuang, and A. V. Shapeev, Comput. Phys. Commun. **258**, 107583 (2021).

[42] W. Li, J. Carrete, N. A. Katcho, and N. Mingo, Comput. Phys. Commun. **185**, 1747 (2014).

[43] X. Huang, L. Yan, Y. Zhou, Y. Wang, H.-Z. Song, and L. Zhou, J. Phys. Chem. Lett. **12**, 525 (2021).

[44] M.-Y. Liu, L. Gong, Y. He, and C. Cao, Phys. Rev. B **103**, 075421 (2021).

[45] W. Zhou, Z. Yang, A. Li, M. Long, and F. Ouyang, Phys. Rev. B **101**, 045113 (2020).

[46] T. Hu, G. Zhao, H. Gao, Y. Wu, J. Hong, A. Stroppa, and W. Ren, Phys. Rev. B **101**, 125401 (2020).

[47] C. Mera Acosta, A. Fazzio, and G. M. Dalpian, npj Quantum Mater. **4**, 41 (2019).

[48] Z. He, R. Peng, X. Feng, X. Xu, Y. Dai, B. Huang, and Y. Ma, Phys. Rev. B **104**, 075105 (2021).

[49] J. Min, C. Zhao, Z. Zeng, Y. Jia, and Z. Du, Phys. Rev. B **100**, 085402 (2019).

[50] L. Xu, M. Yang, S. J. Wang, and Y. P. Feng, Phys. Rev. B **95**, 235434 (2017).

[51] C. Long, Y. Dai, and H. Jin, Phys. Rev. B **104**, 125306 (2021).

[52] Z. Jiang, Z. Liu, Y. Li, and W. Duan, Phys. Rev. Lett. **118**, 266401 (2017).

[53] M. A. Mohebpour, B. Mortazavi, T. Rabczuk, X. Zhuang, A. V. Shapeev, and M. B. Tagani, Phys. Rev. B **105**, 134108 (2022).

[54] A. Patel, D. Singh, Y. Sonvane, P. Thakor, and R. Ahuja, ACS Appl. Mater. Interfaces **12**, 46212 (2020).

[55] M. Zare, B. Z. Rameshti, F. G. Ghamsari, and R. Asgari, Phys. Rev. B **95**, 045422 (2017).